Effects of Martensitic Phase Transformation on Fatigue Indicator Parameters Determined by a Crystal Plasticity Model

John A. Moore [a,*], Jacob P. Rusch[a], Parisa Shabani Nezhad[a], Sivom Manchiraju[b], Dinc Erdeniz[c]

[a] *Department of Mechanical Engineering Marquette University 1515 W Wisconsin Ave, Milwaukee, WI 53233 USA*
[b] *ANSYS, Inc., Southpointe 2600 Ansys Drive Canonsburg, PA 15317 USA*
[c] *Department of Mechanical and Materials Engineering University of Cincinnati 2851 Woodside Drive, Cincinnati, OH 45219 USA*

Abstract

Fatigue indicator parameters are a powerful tool for materials design. These parameters represent the potency of various microstructures to incubate fatigue cracks in metal alloys and are useful in ranking deleterious microstructural features on which to focus process improvements. These fatigue indicator parameters are generally a function of irreversible plastic strain; however, for alloys with solid-state phase transformations (such as Nitinol), reversible transformation strains occur along with plastic strain. This article addresses the question of whether modeling a reversible transformation will affect the predicted value of a fatigue indicator parameter. For Nitinol, the effects of a reversible phase transformation on the fatigue indicator parameter and fatigue life are studied for a polygranular microstructure with and without an inclusion. The crystal mechanics of both plasticity and phase transformations are modeled using the finite element method. It is shown that the usage of a crystal-mechanics-based phase transformation model affects the values of fatigue indicator parameters, the shape of predicted strain–life curves, the distribution of fatigue indicator parameter values in the microstructure, and also the rank ordering of deleterious microstructural features.

Keywords: Nickel–Titanium, Fatigue Indicator Parameter, Crystal Plasticity, Martensitic Phase Transformation

1. Introduction

Fatigue indicator parameters (FIPs) are a powerful tool for materials design [1, 2, 3, 4, 5]. These parameters represent the potency of various microstructural features to incubate fatigue cracks in metal alloys [1, 6] and correlate well to crack tip opening displacement [7]. As such, they can be used to identify and rank deleterious microstructural features on which to focus process improvements [3].

The most commonly used FIPs were not formulated for materials where solid-state phase transformations occur [8, 9, 10, 11]. However, understanding and improving microstructures that affect fatigue resistance is of importance to transforming materials such as superelastic and shape memory alloys used in biomedical applications [12].

Similar to the familiar Coffin–Manson relationship [13, 14, 15], FIPs account for the irreversible deformation that causes fatigue cracks. While some alloys (such as TRIP steels [16]) exhibit predominantly irreversible solid-state phase transformations, superelastic alloys, such as the nickel–titanium alloy Nitinol (NiTi), display transformations that are stress assisted, thermoelastic, and completely reversible (at least in an ideal transformation) [17, 18, 19].

Since models with irreversible plasticity and no transformation are less complex to calibrate, implement, and deploy, the question arises as to whether a reversible transformation affects the value of FIP which only depends on irreversible plasticity.

This article addresses this question and shows the effects of phase transformations on FIP for a superelastic NiTi material.

2. Background

2.1. Fatigue Indicator Parameters

The fatigue life (i.e., the number of cycles until failure, N) of a material is often represented as a function

*Corresponding author
Email address: john.a.moore@marquette.edu (John A. Moore)

of either stress amplitude (S) or plastic strain amplitude ($\Delta\varepsilon^p/2$) and this S–N or $\Delta\varepsilon^p$–N relationship traditionally takes the form of a power law (for example $\Delta\varepsilon^p = AN^b$, where A and b are material parameters). However, observations [10] show that $\Delta\varepsilon^p$–N data differ for torsional and uniaxial loadings. Thus, different FIPs were developed to reconcile this difference. These FIPs are generally related to fatigue life using a form similar to

$$FIP = AN^b, \tag{1}$$

and are dependent on a number of extra calibration parameters along with directional stresses and strains.

As shown by Lankford and Kusenberger [20] and McDowell [1], the fatigue life of metal alloys beyond the initial crack site is often an "inconsequential" fraction of fatigue life. The FIP determined here is meant only to capture this crack incubation life (N) prior to short or long crack growth. This study is also meant only to address crack incubation away from the surface and only high or ultra-high cycle fatigue (similar to [4]). As such, FIPs do not address crack propagation (as in damage tolerant design [15]) or threshold stress ranges for crack propagation (as in the use of a Kitagawa–Takahashi diagram for safe-life design [15]), rather they are used as a tool for determining which microstructure will most deleteriously affect fatigue life (as in Section 5.2). For example, in Robertson et al.'s [21] study, different processing procedures reduce different types of defects (i.e., oxides or carbides). A high quality FIP calculation will show which defect is limiting fatigue life and facilitate the correct selection of one of the processes in [21] to reduce the selected defect's volume fraction.

Of the most common FIPs, are those of Brown–Miller [10], Findley [8], Smith–Watson–Topper (SWT) [9], and Fatemi–Socie [11]. While these are improvements on the $\Delta\varepsilon^p = AN^b$ form, all have limitations. Inaccurate fatigue life predictions occur when using Findley's parameter for non-zero mean stress [22], using SWT for large compressive mean stresses [23], and when using Brown–Miller's parameter for scenarios where cyclic hardening rotates principal stress axes in out-of-phase loadings [11]. The Fatemi–Socie parameter has also proven non-conservative when predicting fatigue life for multiaxial thermomechanical fatigue tests [24]. Since superelastic alloys (especially in biomedical applications) are often used with non-zero mean strain [25], and this work considers materials that harden but are not exposed to thermomechanical cycling, the Fatemi–Socie FIP is used exclusively in this work.

While the common FIPs were derived based on macroscale mechanical state, with the advent of microscale crystal plasticity models [26] and the computational power to perform such calculations using the finite element method (or other similar methods), these FIPs were extended to predict fatigue life based on simulations of the microscale mechanical state of a material [27]. These microscale models predict the anisotropic stress- and strain-state around heterogeneous features such as inclusions [2, 6, 4, 28], voids [2, 4], and grain boundaries [29, 30, 31]. These computational models have shown that FIPs correlate well with the change in crack tip opening displacement and thus FIPs can be viewed as indicators of fatigue crack driving force [7]. From these mechanical state predictions, FIP values are calculated for various microstructural features.

McDowell et al. [32, 29] introduces a length scale to the Fatemi–Socie FIP and determines its value through computational plasticity simulations (using the finite element method) as is employed in this work. The ability to model and predict FIP values allows for a tool for materials design as outlined above.

FIPs have been implemented before to model the fatigue of NiTi [33, 4, 34, 35], but these studies do not address how martensite volume fraction affects fatigue life. One team has set out to model the cyclic properties of NiTi [36] where residual martensite is captured, but do not use the model to predict fatigue life of NiTi. The study in [37] experimentally investigates fatigue of NiTi and discusses the importance that volume fraction of martensite has on fatigue life and that fatigue cracks appear to initiate mainly from voids, impurities, and inclusions such as TiC particles.

2.2. Phase Change in Alloys

Superelastic NiTi alloys are commonly used in biomedical applications but are prone to fatigue failures [25, 38, 21, 12]. These alloys obtain superelasticity (i.e., large recoverable strain) via thermoelastic, stress-assisted, austenite-to-martensite transformations [17, 18, 19]. This behavior is particularly important for biomedical stents that are *crimped* to insert in an angioplasty tube (resulting in a large strain) and as the *crimp* is released the strain reduces and the material is cyclically loaded via the pulsing of blood vessels [25, 38, 21, 12].

While this transformation is ideally recoverable and absent of any dislocation formation [19], this ideal transformation is rarely achieved. Pelton [39] suggests that, under stent loading conditions, the motion of martensite interfaces causes interfacial dislocations which, upon further cycling, become "tangled, shorter,

and more curved" and subsequently impede further motion of the martensite interface. The effect of these stationary interfaces are illustrated in Figure 1 where the hysteresis due to transformation and slip decreases over time leaving what appears to be only hystereses due to plasticity as indicated by the continued increase in mean strain after many cycles.

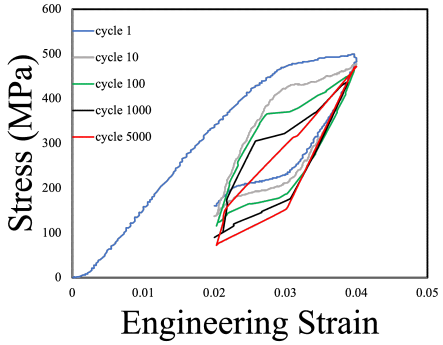

Figure 1: Cyclic response of a superelastic NiTi wire, cycled under 2–4% a strain-controlled condition.

Figure 1 shows the cyclic response of a 0.230 mm superelastic NiTi wire. The material used in this study is a 55.8 wt.%Ni-Ti wire that was purchased from Confluent Medical Technologies. The wire is cycled under 2–4% strain-controlled condition and a frequency of 0.1 Hz, using a Mark10-ESM750 test stand and MR01-50 load cell. The strain range is similar to that studied in [25].

Since an ideal transformation in superelastic NiTi forms no irrecoverable dislocations (dislocations which in turn lead to fatigue failure [15]) and a non-ideal transformation forms martensite interfaces that eventually become stationary, the question arises of whether transformation models are needed in determining FIPs for transforming materials. While a properly calibrated model containing the most physical mechanisms possible has appeal from a predictive standpoint, this predictive power comes with some overhead. For example, the combined transformation and crystal plasticity model used in this work [40] couples the crystal plasticity model of Peirce et al. [41] with the crystallographic phase transformation model of Thamburaja and Anand [42]. If only plasticity is modeled, then roughly 12 parameters need to be calibrated or determined experimentally, if transformation is included, that number increases to 22 parameters. Adding transformation also increases the number of equations that must be solved and thus the computational expense. In the authors' opinion, adding transformation makes the constitutive equations more prone to: becoming stiff numerically, implementation difficulties, convergence issues, and overfitting if parameters are calibrated rather than determined experimentally. Thus, if phase transformation has little or negligible effects, it will be more efficient to neglect it in modeling FIPs.

Cracks that will ultimately cause fatigue failure can form at a variety of microstructural features such as grain boundaries, surface defects, and inclusions [1]. Likewise, for an initially austenite NiTi microstructure, martensite will either begin to form in preferential grains (see Figure 2) or at stress risers such as nonmetallic inclusions [43]. This work will study the effects of martensite that forms in a polygranular microstructure with and without an inclusion.

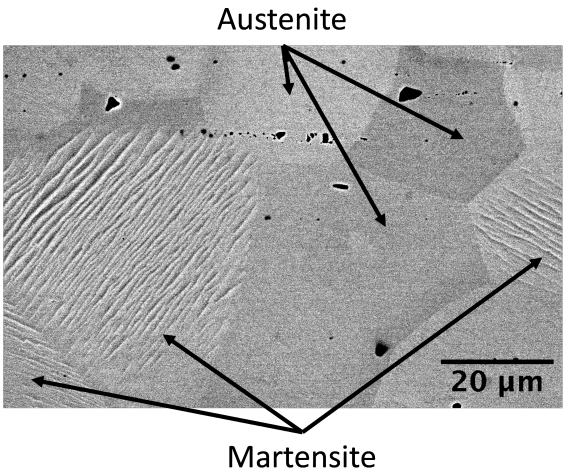

Figure 2: Scanning electron microscope image of the grain structure, the favorably oriented grains are the first to be transformed to martensite under load.

3. Theory

3.1. Fatigue Indicator Parameter

Castelluccio and McDowell [44, 45] proposed a crystallographic version of the Fatemi–Socie FIP defined by

$$FIP^{(\alpha)} = \frac{\Delta\gamma_p^{(\alpha)}}{2}\left(1 + \kappa\frac{\sigma_n^{(\alpha)}}{\sigma_y}\right), \tag{2}$$

where, for a slip system α, $\Delta\gamma_p^{(\alpha)}$ is the change in plastic shear strain [1], $\sigma_n^{(\alpha)}$ is the stress normal to this slip system, σ_y is the yield strength, and κ is a constant determined to equate FIP for uniaxial and torsional loaded specimens [11]. This value is calculated for each slip

system and the maximum value over all the slip systems is stored. Here $\kappa = 0.55$ which is an average of the value of 0.5 used in [45] and the value of 0.6 used in [11]. The value of σ_y is 750 MPa for the austenite. This yield stress is observed in single cycle simulations of the microstructure in Figure 3 without transformation. To account for size effect, the FIP value in Equation 2 is nonlocal. The FIP value is calculated at every material point and averaged over a region 10% of the volume of either a grain or the inclusion in accordance with the procedure in [6] [1].

The plastic shear strain is calculated by projecting the plastic strain tensor $\boldsymbol{\varepsilon}^p$ onto the slip direction $\mathbf{s}^{(\alpha)}$ and slip plane normal $\mathbf{n}^{(\alpha)}$ respectively

$$\gamma_p^{(\alpha)} = \mathbf{s}^{(\alpha)} \cdot \boldsymbol{\varepsilon}^p \cdot \mathbf{n}^{(\alpha)}. \tag{3}$$

Similarly, the stress normal to a slip plane is a function of the Cauchy stress $\boldsymbol{\sigma}$ and is determined by

$$\sigma_n^{(\alpha)} = \mathbf{n}^{(\alpha)} \cdot \boldsymbol{\sigma} \cdot \mathbf{n}^{(\alpha)}. \tag{4}$$

As shown in [4], the value of FIP will begin to saturate at a constant value after a number of cycles. This number of cycles is often five or less [31, 4, 34]. Five cycles are used in this work.

3.2. Constitutive Model

The constitutive model is the same as that proposed by Manchiraju and Anderson in [40] and is implemented using an Abaqus user material (UMAT). It accounts for rate dependent plasticity in the B2 austenite crystals as well as rate independent transformation between austenite and B19′ martensite. The plasticity is irreversible, the transformation is completely reversible (although the transformation will be *locked in* in this study to compare simulations with and without transformation). The material parameters are identical to those used in [40] with the only exception that the martensite elastic moduli are set to half of the austenite elastic moduli (as was used in [47]). A detailed description of the model is given in [40, 48] Appendix B and only a summary of the fundamental equations of the model are given here.

The deformation gradient is multiplicatively decomposed into an elastic ($\mathbf{F}^e$) and inelastic ($\mathbf{F}^{\text{inel}}$) part

$$\mathbf{F} = \mathbf{F}^e \cdot \mathbf{F}^{\text{inel}}. \tag{5}$$

[1] Example input decks and post-processing scripts are available at [46]

The corresponding inelastic velocity gradient ($\mathbf{L}^{\text{inel}}$) further decomposes the deformation rate into that formed via plasticity and that formed via transformation

$$\mathbf{L}^{\text{inel}} = v_A \sum_{\alpha}^{N_S} \dot{\gamma}_p^{(\alpha)} \mathbf{S}_{\text{Slip}}^{(\alpha)} + \sum_{\beta}^{N_T} \dot{v}^{(\beta)} \mathbf{S}_{\text{Trans}}^{(\beta)}, \tag{6}$$

where v_A is the volume fraction of austenite and $v^{(\beta)}$ is the volume fraction of a martensite variant β, N_S is the number of slip systems in the austenite, and N_T is the number of martensite variants. The two Schmid-type tensors are given by $\mathbf{S}_{\text{Slip}}^{(\alpha)} = \mathbf{s}^{(\alpha)} \otimes \mathbf{n}^{(\alpha)}$ and $\mathbf{S}_{\text{Trans}}^{(\beta)} = \mathbf{b}^{(\beta)} \otimes \mathbf{m}^{(\beta)}$ where $\mathbf{b}^{(\beta)}$ is a displacement vector for an invariant plane with normal $\mathbf{m}^{(\beta)}$.

The unknown quantity characterizing plastic deformation is the plastic shear strain rate defined by

$$\dot{\gamma}_p^{(\alpha)} = \dot{\gamma}_0 \left(\frac{\tau^{(\alpha)}}{\tau_0^{(\alpha)}} \right)^{\frac{1}{m}} \operatorname{sign}\left(\tau^{(\alpha)}\right), \tag{7}$$

where $\dot{\gamma}_0$ is a reference slip rate, $\tau^{(\alpha)}$ is a resolved shear stress on the slip system, and $\tau_0^{(\alpha)}$ is the slip system strength. The slip system strengths harden in accordance with a hardening law that accounts for a saturation stress and for self and latent hardening as described in [40].

The unknown quantity characterizing inelastic deformation due to transformation strain is the volume fraction of each martensite variant which evolves in accordance with

$$-f_c \leq f^{(\beta)}\left(v^{\beta}, \boldsymbol{\sigma}, \theta\right) \leq f_c, \tag{8}$$

where f_c is the critical driving force for transformation and $f^{(\beta)}$ is the driving force for transformation, θ is the temperature. Equation 8 accounts for both forward and reverse transformation when $f^{(\beta)}$ is outside the bounds set by $\pm f_c$. The driving force is given by

$$\begin{aligned} f^{(\beta)} &= \varepsilon_T^{(\beta)} \left(\mathbf{b}^{(\beta)} \cdot \left(\mathbf{F}^{e^T} \cdot \mathbf{F}^e \cdot \boldsymbol{S} \right) \cdot \mathbf{m}^{(\beta)} \right) \\ &- \frac{\lambda_T}{\theta_T} (\theta - \theta_T) - \sum_{\delta}^{N_T} \mathbf{h}_{\beta\delta} v_\delta \end{aligned} \tag{9}$$

where $\varepsilon_T^{(\beta)}$ is the transformation strain, $\boldsymbol{S}$ is the second Piola–Kirchhoff stress, λ_T is the latent heat of transformation per unit volume, θ_T is the equilibrium transformation temperature, and $\mathbf{h}_{\beta\delta}$ is the martensite variant compatibility.

4. Finite Element Model

This work studies two types of microstructure: a polygranular microstructure and a polygranular mi-

crostructure with a stiff inclusion (representing a non-metallic inclusion in a NiTi material). The finite element mesh for each of these microstructures are shown in Figure 3 and Figure 4 respectively. The grain structure for each mesh is created using Neper software and Laguerre tessellation [49, 50, 51]. The polygranular mesh has 64,000 elements and 68,921 nodes (similar to [35]). The polygranular mesh with an inclusion has 97,184 elements and 103,135 nodes. Eight node hexahedral elements with reduced integration are used exclusively. Abaqus (2018) finite element software is used for implicit simulations. While this regular mesh may produce some elastic stress concentrations at grain boundaries, these concentrations will be reduced as inelastic deformations form. The displacement on faces with normals in the negative directions are fixed in x-, y-, and, z-directions respectively. Each of the free edges is held flat using constraint equations. The microstructure is loaded in the x-direction with a displacement and the y- and z-directions contract/extend accordingly based on the material's apparent Poisson's ratio. Each mesh has 100 equiaxed crystallographic grains with constant Euler angles inside each grain. The mesh with the inclusion has the same grain shape and orientations as the mesh without the inclusion. This is considered a statistical volume element (SVE), the statistics of which are discussed later in this article. The texture of the Euler angles is random and is generated by creating randomly distributed quaternions and then converting them to Euler angles. While, cold drawn wire, tubes, and plate NiTi—from which devices like biomedical stents are made—often have a crystallographic texture, the strength of the texture can vary. So, as to not address a specific texture, a random texture is considered here. The inclusion is considered linear elastic with a Young's modulus of 200 GPa and a Poisson's ratio of 0.3, and it is fully bonded to the matrix material. The inclusion is centered and accounts for 1% of the microstructure volume.

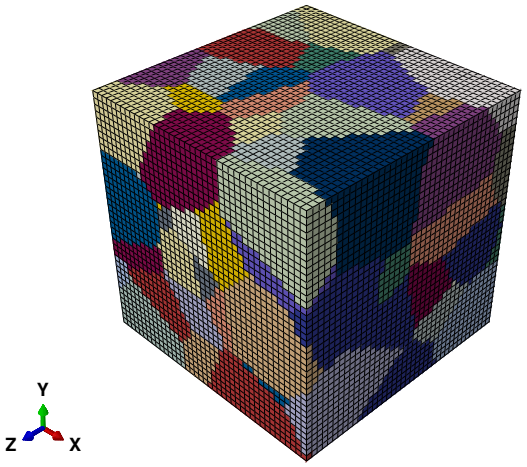

Figure 3: The finite element mesh of the polygranular microstructure. The colors represent different crystallographic grains.

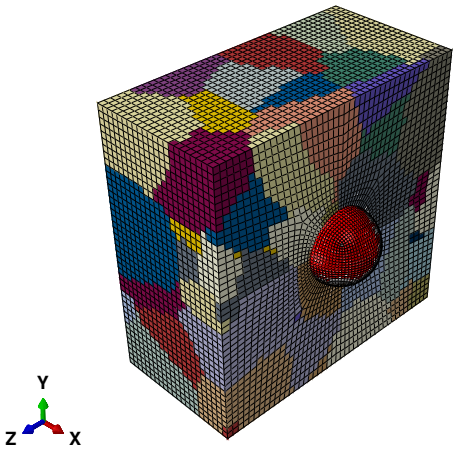

Figure 4: The finite element mesh of the polygranular microstructure with a stiff inclusion. The colors represent different crystallographic grains and the red center sphere is the inclusion. Only half of the mesh is shown to highlight the center inclusion.

The nonlocal FIP calculated in Equation 2 is averaged over a volume. For this work, predetermined volumes are selected for this average as shown in Figure 5 and Figure 6. Absolute values of the length scale of this volume are suggested by various authors [52, 2, 28] to range from 0.3–3 μm while others base the length scale on the volume of slip planes in crystallographic planes [45]. Other authors [6, 4] suggest a relative value of 10% of the length scale of the microstructural features of interest; this approach is used in this work.

For the polygranular microstructure and polygranular microstructure with inclusion, the volume over which the FIP is averaged is 0.1% of the total volume, this corresponds to 10% of the grain and inclusion volumes respectively.

To study the microstructure without transformation, the value of $\varepsilon_T^{(\beta)}$ in Equation 9 is set to zero and the value of f_c in Equation 8 is set to be large. To study the microstructure with phase transformation, the martensite volume fraction is locked in by a prestrain without plasticity (where $\dot{\gamma}_0 = 0$ in Equation 7) then the applied strain is removed until the stress-free strain is achieved. The mean strain and strain amplitude is then applied in addition to the stress-free strain without transformation,

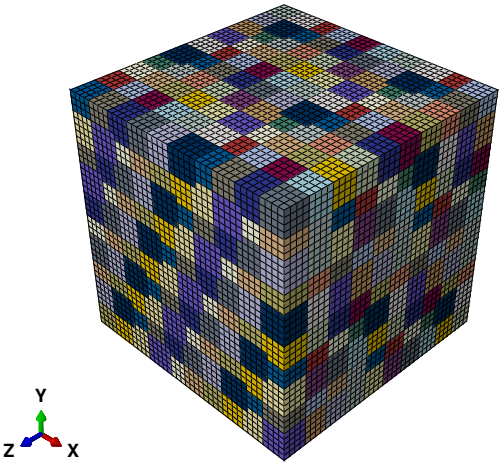

Figure 5: The finite element mesh of the polygranular microstructure. The colors represent different volumes over which FIP is averaged.

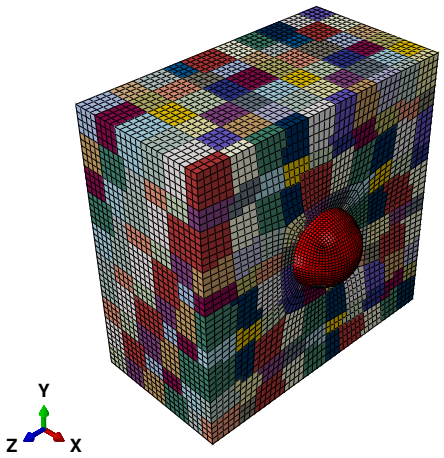

Figure 6: The finite element mesh of the polygranular microstructure with a stiff inclusion. The colors represent different volumes over which FIP is averaged. Only half of the mesh is shown to highlight the center inclusion.

but with residual martensite as shown in Figure 7.

5. Results and Discussions

5.1. Polygranular Microstructure

Two strains determine the fatigue life and FIP for a microstructure: the mean strain and the strain amplitude ε_a. Here a mean strain is chosen and then the FIP is studied for a range of strain amplitudes. Using a simulation with only plasticity and no transformation, the effects of mean strain are shown in Figure 8. For Figure 8 and all subsequent figures, plotted points represent results for the maximum volume averaged FIP, and connecting lines represent a linear interpolation between simulations points. In Figure 8 the FIP value is plotted against mean strain for several values of strain amplitude which are represented by the color gradient in the colorbar. The purpose of Figure 8 is to stratify the effects of mean strain and choose a mean strain for this study. In Figure 8, four regions representing different behavior of FIP (with respect to mean strain) are identified. The regions depend on the behavior of the microstructure during the lowest and highest strain of the cyclic loading. In the red region (lower left of Figure 8), the lowest and highest strain both cause limited or no hardening of the material and the FIP value increases proportional to the stress increase. In the yellow region (lower right of Figure 8), both the lowest and highest strain cause hardening of the material and the FIP value is mostly influenced by plastic strain. In the blue region (upper part of Figure 8), for zero mean strain, the strain amplitude is large enough that the lowest strain can cause hardening in compression while the highest strain also causes hardening in tension. The result is that, as the mean strain increases, the lowest strain causes progressively less hardening and eventually a nearly elastic response. The is why the FIPs in the blue region decrease with mean strain. Finally, in the small green region (left part of Figure 8), the lowest and highest strain are in a transition range that causes limited hardening. This work studies only the yellow and blue regions where plasticity drives the FIP performance; thus, a mean strain of 1% is chosen to avoid the red and green region with limited hardening and plastic strain. The results of this study should be interpreted only for the FIP behavior in the yellow and blue regions.

At 1% mean strain, the effect of phase transformation and residual martensite is studied. A prestrain of 2%, 3.4%, and 4.4% (without plasticity) lock in global martensite volume fractions of 25%, 50%, and 65% respectively. The microstructure with these martensite volume fractions are shown in Figure 9 and the stress needed to produce this volume fraction of martensite is shown in Figure 10. The effects of these martensite volume fractions on FIP are shown in Figure 11. Figure 11 shows that, for a given strain amplitude (above ~1.0%), the presence of residual martensite lowers the FIP value (and thus, increases fatigue life). For a strain amplitude of 0.5%, the distribution of FIP in the microstructure is shown in Figure 12. Figure 12 shows that for 25% martensite volume fraction there is a limited redistribu-

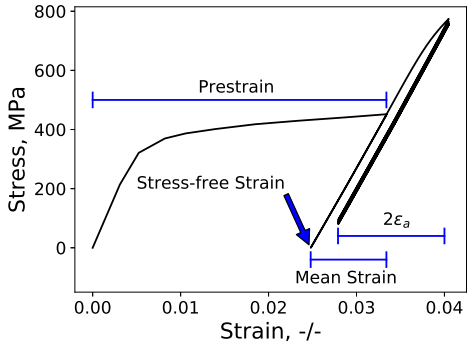

Figure 7: The prestrain that locks in martensite, the stress-free strain after load is released, the mean strain, and two times the strain amplitude ε_a of the cyclic strain are shown.

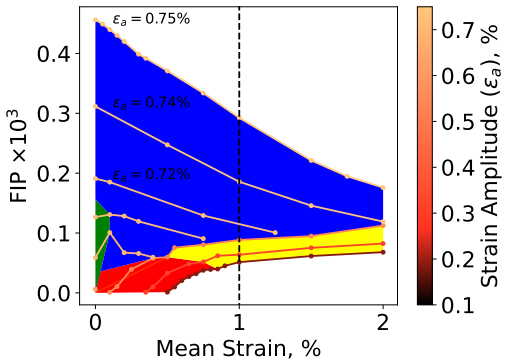

Figure 8: The effect of mean strain on FIP. Four regions representing different behavior of FIP (with respect to mean strain) are identified in red, yellow, green, and blue background colors. The mean strain at which further simulations are performed is highlighted by a dashed vertical line.

tion of FIP, but for 50% and 65% martensite volume fraction the FIP values are redistributed more dramatically and are much more localized. Thus, for larger volume fractions, the presence of martensite not only changes the value of FIP it also changes the distribution within the microstructure.

Figure 11 also shows two distinct regions in each curve, a more horizontal region in the upper part of the figure where FIP increases quickly as strain amplitude increases and a more vertical part of the curves where FIP is less sensitive to strain amplitude increase. Behavior of FIP in the vertical region is difficult to see in Figure 11, so a zoomed-in view of the vertical region for each martensite volume fraction is shown in Figure 13.

Figure 13 shows that the presence of martensite elongates the vertical region where FIP is less sensitive to strain amplitude. However, Figure 13 also shows that there is a region, for each martensite volume fraction, where FIP decreases with increased strain amplitude. This means that a higher strain amplitude results in a larger fatigue life. While this may seem counterintuitive, the reason for this is that these simulations are strain controlled. Being strain controlled, the R ratio (of minimum to maximum stress) is not constant. The decrease in FIP with increased strain amplitude occurs in the region where R ratio transfers from positive to negative. This is possibly due to a limited increase in plastic strain near a minimum stress value of zero (as illustrated in Equation 7). Figure 14 uses Equation 1 to convert fatigue lives at various R ratios to FIP values; in Equation 1, $A = 0.6482$ and $b = -0.5952$ are used to convert experimentally observed fatigue life to FIP. Fatigue lives from the MMPDS handbook for several aluminum alloys and one nickel-superalloy (Inconel 718) show that this local minimum of FIP near a R ratio of zero is both possible and also observed at some stress levels in some alloys. Figure 15 combines the FIP values for strain amplitudes of less than 1%. Figure 15 shows that FIP values does not monotonically decrease with increasing martensite volume fraction for strains amplitudes of less than 1%. At the lowest strain amplitude, the FIP values from simulations with 0% and 25% martensite volume fraction are similar and then FIP decreases as martensite volume fraction increases. For strain amplitudes from 0.25% and 0.5%, the FIP values from simulations with 0% and 50% martensite volume fraction are similar. For strain amplitudes from 0.5% and 1.0%, nearly all permutations of FIP versus martensite volume fraction are observed (i.e., FIP does not decrease monotonically with an increase martensite volume fraction). For example, at 0.6% strain amplitude, the lowest FIP is for either 0% or 65% martensite volume fraction and the highest FIP is for 50% martensite volume fraction; whereas, at 0.7% strain amplitude the FIP goes from lowest to highest for 0%, 25%, 65%, and 50% martensite volume fraction respectively.

As mentioned above, the 100 grain microstructure is considered an SVE. To evaluate the statistics of such a microstructure, 20 realizations of the 100 grain microstructure are considered. Each realization has different grain orientations extracted from a random texture orientation distribution, and has random equiaxed grain centroid locations. The results are shown in Figure 16. Figure 16 shows that the FIP value of each volume fraction of martensite has some spread. This entire spread is what is plotted for the error bars in Figure

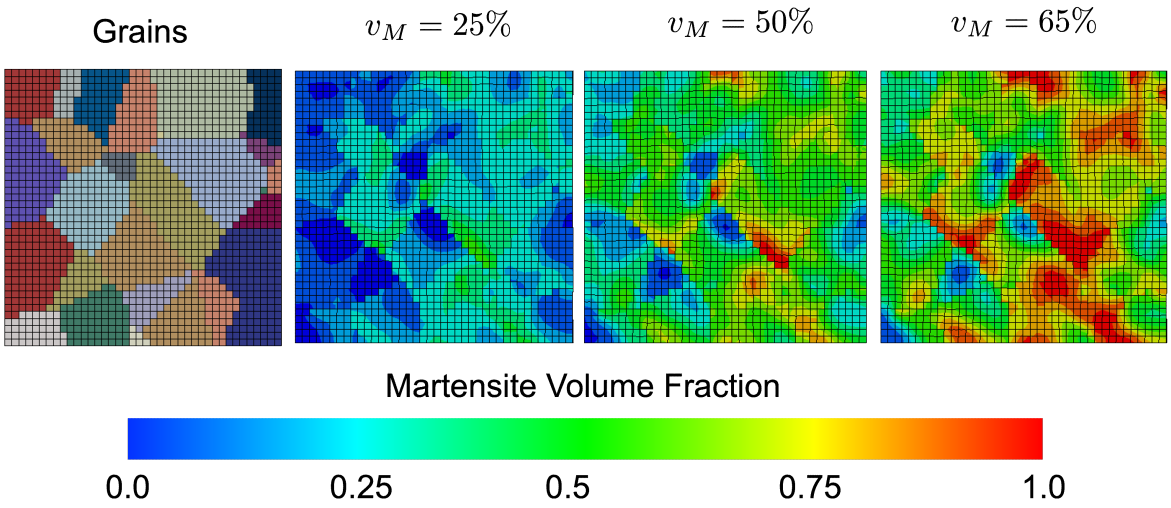

Figure 9: From left to right are shown the grain structure of the material then the local martensite volume fraction for 25%, 50%, and 65% global martensite volume fraction. Each image slice is in the $x-y$ plane at the center of the microstructure in the z-direction.

11. The microstructure with 50% and 65% martensite have some overlap in FIP values whereas the FIP values for the other microstructures do not. The largest spread in FIP values is for the microstructure without martensite, the lowest spread is for the microstructure with 50% (i.e., a spread in FIP of 1.27×10^{-3}), but the spread for 65% martensite is also low (i.e., a spread in FIP of 1.95×10^{-3}). While interaction between plastic strain in all grains is possible without martensite, the martensite is not considered to deform plastically in this model, so grain interactions favorable to fatigue nucleation are also limited. The highest FIP value for the 65% martensite structure in Figure 11 may indicate this interaction occurring is some realizations such that the highest FIP is separated from the majority of the distribution. However, this spread is small enough (for the number of realizations considered) to indicate that the FIPs with martensite and without martensite are statistically different, even if different realizations of microstructure are considered.

While Figure 11 shows that the presence of martensite has a non-negligible effect on the FIP values predicted by simulations, it is possible that when the coefficients in Equation 1 are fit to fatigue life data that the set of FIPs for each volume fraction of martensite produce the same fatigue life curve—just with different coefficients A and b from Equation 1. For example, if the values of FIP in the four curves in Figure 11 where simply multiples of each other, then when converted to fatigue life, all four curves would produce the same strain–life curve. The purpose of Figure 18 is to show that this is not the case the FIP curves in Figure 11. To produce Figure 18, the values of A and b from Equation 1 are fit (using Matlab's `fminsearch` and least squares regression) to the superelastic NiTi fatigue data from Pelton et al. [25]. Details of this fitting procedure are shown in Appendix A. First, using the Coffin–Manson relationship $\Delta\varepsilon^p = AN^b$, a curve is fit to the data and shown in Figure 17. Then, the FIP values for each martensite volume fraction microstructure are fit to the Pelton data curve using Equation 1 in Figure 18. Since Pelton et al.'s data is for constant R ratio, the region where FIP decreases with increased strain are omitted in Figure 18.

In Figure 18, the predicted fatigue life for each volume fraction of martensite follows the overall trend seen by the average data in Figure 17—where there are two vertical regions to each curve connected by a horizontal region. However, the length and slope of each region varies based on the amount of martensite. With zero martensite, the lower strain vertical region is the smallest (of the four martensite volume fractions studied) and the horizontal region has the lowest slope and is the longest. With 65% martensite volume fraction, the higher strain vertical region is the smallest and has the lowest slope (of the four martensite volume fractions studied). The 25% and 50% martensite volume fraction microstructures show behavior transitioning between that of the 0% and 65% martensite microstructures. This shows that, even with different fitting parameters, the presence of martensite affects the fatigue life predictions for polygranular superelastic NiTi mi-

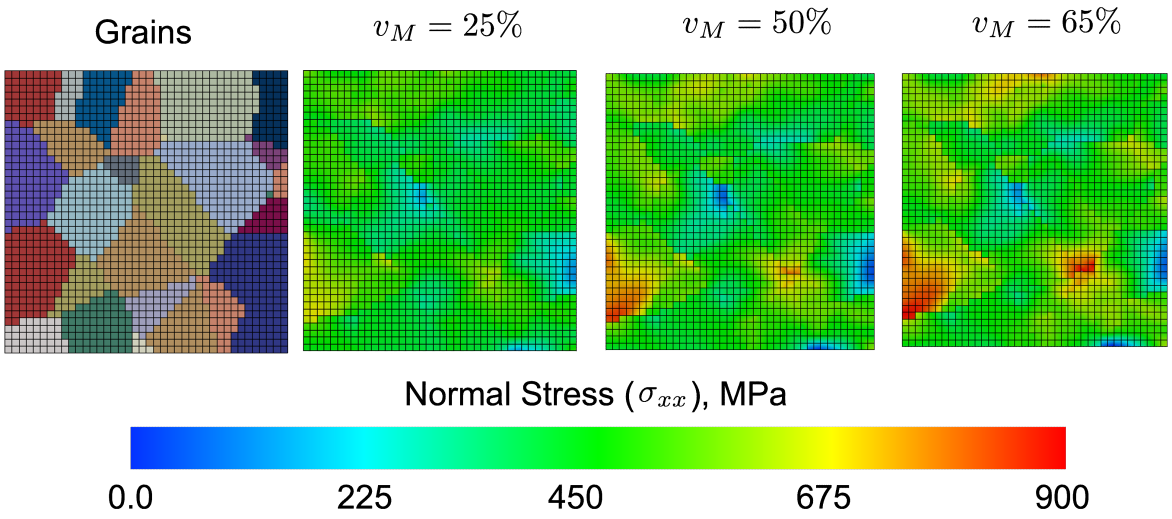

Figure 10: From left to right are shown the grain structure of the material then the normal stress in the x-direction produced from the load needed to induce 25%, 50%, and 65% global martensite volume fraction. Each image slice is in the $x-y$ plane at the center of the microstructure in the z-direction.

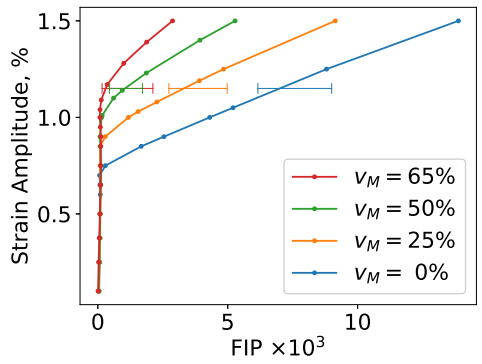

Figure 11: FIP values at various strain amplitudes and global martensite volume fractions. The mean strain for all simulations is 1%. The error bars represent the entire spread in 20 realization of the sample at 1.15% strain amplitude.

crostructures.

For the results shown above, there is a microscale distribution of martensitic volume fraction (see Figure 9) which is induced by a tensile prestrain. However, there is a sub-microscale distribution of active/inactive martensite variants at each point as well. For the tensile prestrain applied above, approximately six martensite variants are active for each point (some points indicate a very small volume fraction is a seventh variant). The remaining 18 variants are inactive. A prestrain in compression activates six different variants. While six variants are activated via a uniaxial applied pre-strain, all variants are activated if variants are temperature induced. To study the effect of activating all variants, the constant temperature of 257 K used above is replaced with a ramped temperature. The temperature is ramped from 0 K to 276.50, 273.5, 271.6 K, to induce 25%, 50%, 65% martensite volume fraction respectively. Replacing the prestrain with this temperature ramp and then cycling at a mean strain of 1% and a strain amplitude of 1.5% give the results in Figure 19. In Figure 19, it shows that the global volume fraction of martensite still reduces the FIP values; however, that reduction is more dramatic in the larger volume fractions range. This shows that transformation effects the FIP with different number of active variants and that the model used here predicts that fatigue life will be longer if more martensite variants are active (for > 50% global volume fraction of martensite).

5.2. *Microstructure with Inclusion*

The inclusion causes a stress concentration factor K_t. The effective homogeneous Young's modulus from the polygranular simulations (as shown in Figure 7) is 68752 MPa. This is used in a homogeneous linear elastic simulation, the results of which are shown in Figure 20. From the results shown in Figure 20, the stress concentration factor is $K_t = 1.53$; this stress concentration factor adds an extra driving force to form plastic strain. This linear elastic stress concentration factor also amplifies the applied strain. While a 1% mean strain is

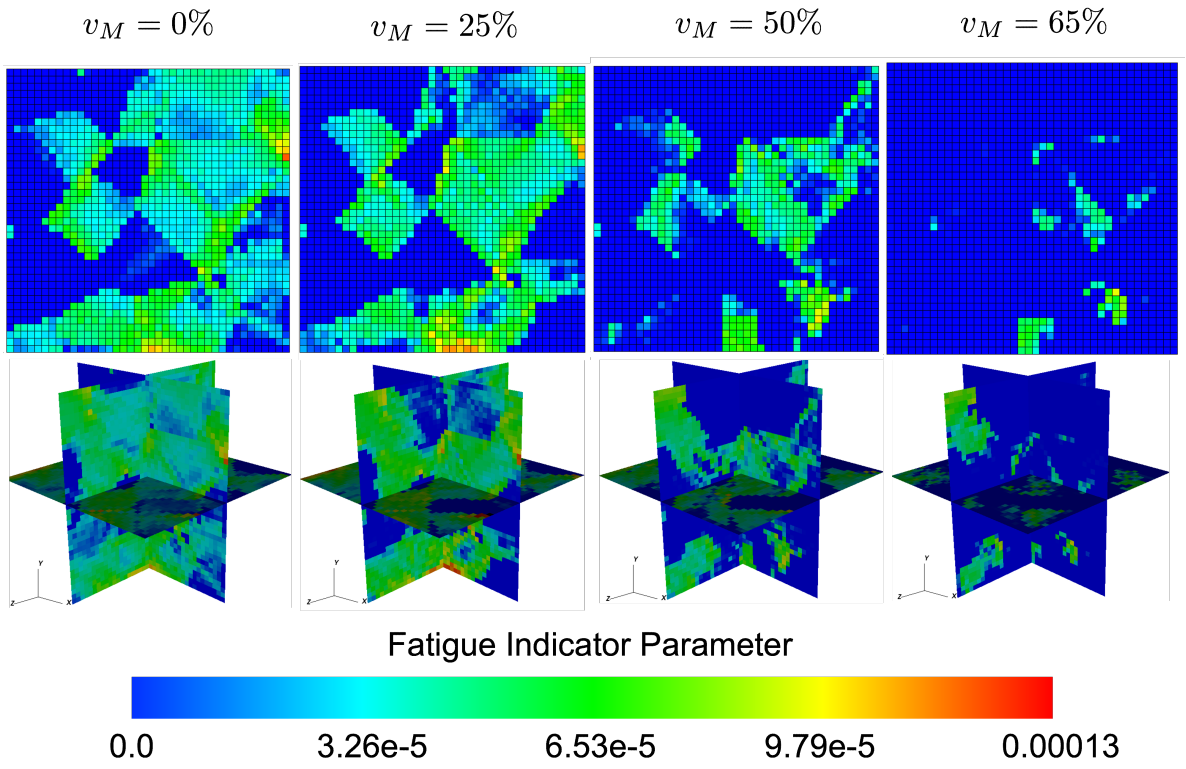

Figure 12: From left to right are shown the local FIP values for 0%, 25%, 50%, and 65% global martensite volume fraction loaded with 1% mean strain and 0.5% strain amplitude. Each image slice in the top row is in the $x-y$ plane at the center of the microstructure in the z-direction. Three planes slice the center of the structure in the bottom row.

applied to the inclusion simulations, the elastic strain around the inclusion is closer to 1.53%; however, this mean strain still falls in the blue and yellow region of Figure 8, so these simulations account for similar cyclic behavior to the polygranular simulations.

At 1% mean strain, the effect of phase transformation and residual martensite is studied. A prestrain of 1.3%, 2%, and 3.4% (without plasticity) lock in global martensite volume fractions of 12.5%, 25%, and 50% respectively. The microstructure with these martensite volume fractions are shown in Figure 21 and the stress needed to produce this volume fraction of martensite is shown in Figure 22. For a strain amplitude of 0.5%, the distribution of FIP in the microstructure is shown in Figure 23. Figure 23 shows that, for 12.5% and 25% martensite volume fraction, there is a limited redistribution of FIP as compared to the structure without martensite, but, for 50% martensite volume fraction, the FIP values are redistributed more dramatically and are much more localized. For 50% martensite volume fraction, the peak FIP value moves closer to the inclusion; whereas, at lower volume fractions the peak value is offset from the inclusion. In all cases, the peak FIP value is in the region of stress concentration, but for 50% martensite volume fraction the peak FIP is more isolated to that high stress region. Thus, for larger volume fractions of martensite, the presence of martensite not only changes the value of FIP it also changes the distribution within the microstructure.

Figure 25 shows that, for a given strain amplitude, the presence of residual martensite lowers the FIP value in a similar fashion to the polygranular simulations without an inclusion. The overall behavior of FIP is very similar with both microstructures. Thus, the previous discussion of these curves for the polygranular structure holds for the inclusion as well.

Then, the FIP values for each martensite volume fraction microstructure are fit to the Pelton data curve using Equation 1 in Figure 24 using the same procedure as in Figure 18. The life curves in Figure 24 show a similar trend to those without the inclusion for higher strain. For low strain, the life predictions are very similar for all volume fractions. This may be the effect of the elastic stress concentration factor from the inclusion driv-

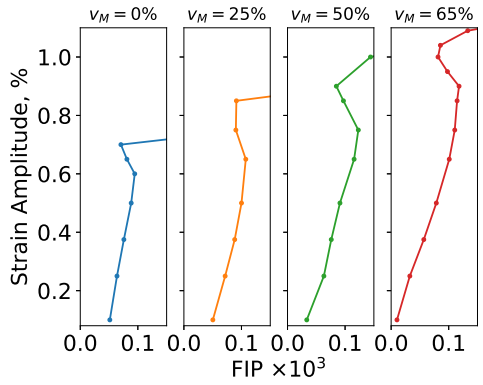

Figure 13: The behavior of FIP for lower values of FIP at various strain amplitudes and global martensite volume fractions. The mean strain for all simulations is 1%.

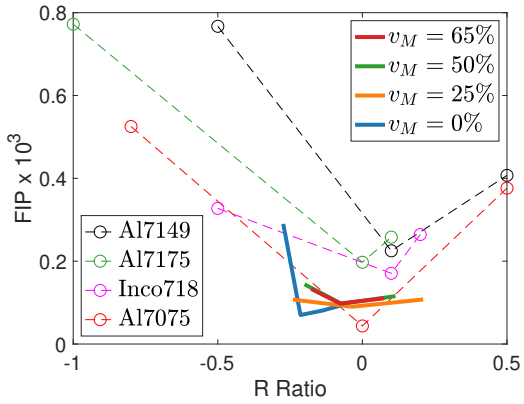

Figure 14: Fatigue indicator parameters from MMPDS [53] (using Equation 1 with $A = 0.6482$ and $b = -0.5952$) at a constant stress amplitude for hand forged and notched Al 7149-T73, extruded Al 7175-T73511, sheet Inconel 718, and sheet Al 7075-T6. The experimental values are compared to simulations results.

ing the fatigue value regardless of the martensite volume fraction.

For the microstructure without martensite, the inclusion causes the FIP to be higher (and the fatigue life to be lower) than without the inclusion. For the 25% and 50% martensite volume fractions, the presence of the inclusion lowers the FIP value. This effect is likely due to the *shielding* near inclusions simulated in [54] for NiTi with non-zero mean strains.

For each different martensite volume fraction, the effect of the inclusion on FIP (as compared to without the inclusion) differs, and thus, the presence of martensite changes how each microstructure is ranked in terms of potency for incubating fatigue cracks.

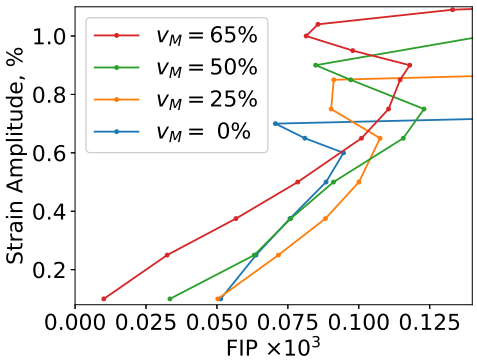

Figure 15: Combined lower values of FIP at various strain amplitudes and global martensite volume fractions. The mean strain for all simulations is 1%

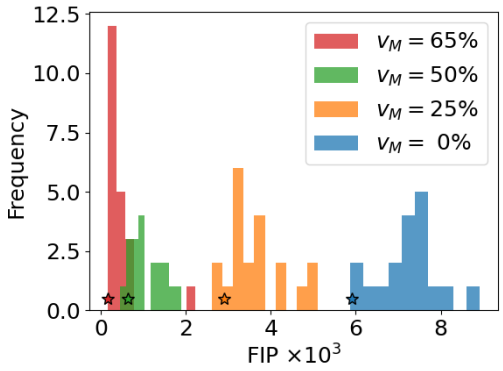

Figure 16: The FIP value for 20 realiziations with a mean strain of 1% and a strain amplitude of 1.15%. The stars indicate the microstructure used in and Figure 11 and Figure 13. The bars are plotted with some transparency so overlap is evident.

6. Summary and Conclusions

6.1. Summary

As shown in Figure 11 and Figure 25, a transformation model affects the value of FIP. As shown in Figure 18, a transformation model also affects fatigue life and the shape of the predicted $\Delta\varepsilon$–N curve. Figure 15 shows that, for lower strain amplitudes, there is not a monotonically decreasing relationship between FIP and increasing martensite volume fraction. Also, as shown in Figure 25, a transformation model affects the rank ordering of deleterious microstructural features. The presence and volume fraction of martensite affects not only the value of FIP but also its distribution in the microstructure as shown in Figure 12 and Figure 23. Finally, the

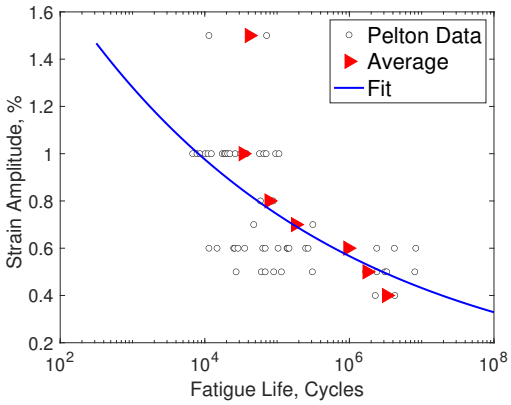

Figure 17: Pelton et al. [25] superelastic NiTi fatigue data for non-zero means strain. A fit to the data using the Coffin–Manson relationship and the average fatigue life at every strain amplitude are shown.

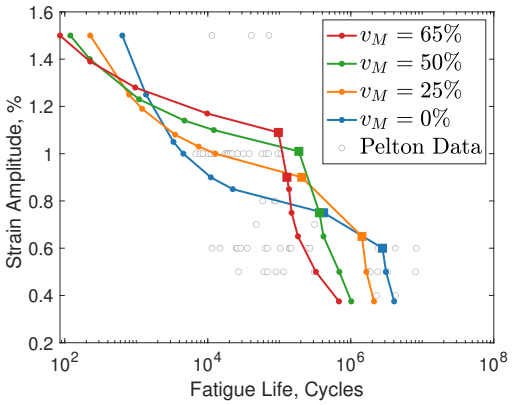

Figure 18: FIP values fit to Pelton et al.'s data [25]. The data between the square markers shows an increase in fatigue life with increased strain amplitude and is omitted. The connecting line between square datapoint is for visual reference only. For $v_M = 0\%, A = 0.6482,\ b = -0.5952$, $v_M = 25\%, A = 0.1434,\ b = -0.5077$, $v_M = 50\%, A = 0.0497\ b = -0.4687$, $v_M = 65\%, A = 0.0201,\ b = -0.4370$.

number of active martensite variants also affects how FIP changes as martensite volume fraction is increased.

6.2. *Conclusions*

The use of a transformation model affects the overall predictions of FIP and fatigue life. It appears that modeling transformation is valuable and needed for accurate fatigue predictions. This is the case both for microstructures with defects (such as inclusions or voids) as well as defect-free polygranular microstructures. It is especially important to include a phase transformation model when rank ordering of deleterious microstructural features, because the presence of martensite changes this ordering (for the microstructure studied here).

While the conclusion is that: reversible transformation will affect the FIP even though FIP only depends on irreversible plasticity, it is not to say that the transformation model employed here is an accurate model of all of the mechanisms in a NiTi microstructure. The model used here only accounts for reversible transformation and plasticity in the austenite and shows that transformation does affect FIP. Since transformation affects FIP, it is important to model the transformation accurately and perhaps in more detail than is employed here. For example irreversible transformation, ratcheting, and plasticity in the martensite phase (see [36, 55, 56, 57, 58, 59]) will be important to simulate fatigue effectively. Models of the R phase crystal structure [60] are also worth considering.

7. Acknowledgement

This material is based upon work supported by the National Science Foundation under Award Number 1934753. Support was provided by the Division of Civil, Mechanical and Manufacturing Innovation's (CMMI) Mechanics of Materials and Structures (MOMS) program. The authors would also like to thank Professor Peter Anderson of the Ohio State University for his gracious discussions of and generosity with sharing the phase transformation materials model.

Appendix A: fminsearch Details

To determine A and b from Equation 1, Matlab's `fminsearch` command is used with the default options. This command is used to minimize the residual S_r given by

$$S_r = \sum \left[\left(\log\left(N_{data}\right) - log(N_{model}) \right)^2 \right], \qquad (10)$$

where N_{data} is the fit line in Figure 17 and N_{model} is the fatigue life prediction from the simulated FIPs. For all simulations the initial guesses for A and b used in `fminsearch` are A = 5e-5 and b = -5e-1 with the exception of the microstructure with an inclusion and 25% and 50% martensite where A = 0.1434 and b = -0.5077.

Appendix B: Constitutive Model

Details of the constitutive model are given here. They are identical to those is in [40]. The multiplicative de-

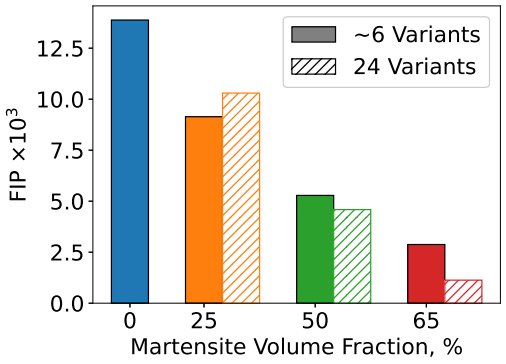

Figure 19: Comparison of prestrained samples with six martensite variants to ramped temperature samples with 24 martensite variants cycling with a mean strain of 1% and a strain amplitude of 1.5%

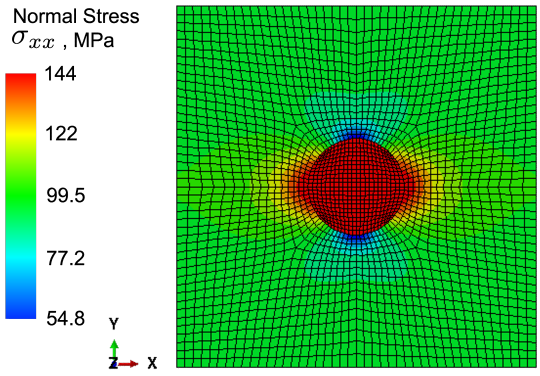

Figure 20: The normal stress contour is shown in an equivalent linear elastic microstructure with an inclusion.The stress concentration at the extreme x-edges of the inclusion is apparent. The image is a slice is in the $x-y$ plane at the center of the microstructure in the z-direction.

composition shown in Equation 5 is used to formulate the deformation gradient rate

$$\dot{\mathbf{F}}^{\text{inel}} = \mathbf{L}^{\text{inel}} \cdot \mathbf{F}^{\text{inel}}. \tag{11}$$

This forms an ordinary differential equation. The solution of which at a current time τ is based on the solution at the previous time t and an approximation of the matrix exponential given by

$$\begin{aligned} \mathbf{F}^{\text{inel}}(\tau) &= \left[\mathbf{I} + v_A \sum_{s=1}^{N_s} \Delta\gamma^{(s)}(\tau)\mathbf{S}^{(s)}_{\text{slip}} \right. \\ &+ \left. \sum_{t=1}^{N_T} \Delta v^{(t)}(\tau)\mathbf{S}^{(t)}_{\text{trans}}, \right] \mathbf{F}^{\text{inel}}(t) \end{aligned} \tag{12}$$

where v_A is the total volume fraction of the austenite phase. From $\mathbf{F}^{\text{inel}}$, the total deformation gradient $\mathbf{F}$ (from the displacement driven finite element method), and Equation 5, the elastic part of the deformation gradient $\mathbf{F}^{\text{e}}$ is determined. From this the elastic Green-Lagrange strain is determined

$$\mathbf{E}^e = \frac{1}{2}\left(\mathbf{F}^{e^T} \cdot \mathbf{F}^e - \mathbf{I}\right). \tag{13}$$

Then the second second Piola–Kirchhoff stress is given by

$$\mathbf{S} = \mathbb{C} : (\mathbf{E}^e - \mathbf{A}_{\text{th}}(\theta - \theta_0)), \tag{14}$$

where θ_0 is a reference temperature, $\mathbb{C}$ is anisotropic elastic modulus and $\mathbf{A}_{\text{th}}$ is the thermal expansion matrix. Both are calculated from the values for martensite and austenite respectively based on a rule of mixtures. The resolved shear stress is given by

$$\tau^\alpha = \mathbf{b}^{(\alpha)}_{\text{Slip}} \cdot \left(\mathbf{F}^{e^T} \cdot \mathbf{F}^e \cdot \mathbf{S}\right) \cdot \mathbf{m}^{(\alpha)}_{\text{Slip}}. \tag{15}$$

The slip system hardness evolves based on

$$\tau_0^{(\alpha)} = \sum_{r=1}^{N_s} h^{(r)}\left(Q + (1-Q)\delta_{(\alpha r)}\right)|\dot{\gamma}^{(r)}|, \tag{16}$$

where Q is the ratio of self to latent hardening, $\delta_{(\alpha r)}$ is the Kronecker delta and

$$h^{(r)} = h_0\left(1 - \frac{\tau_0^{(r)}}{\tau_0^{\text{sat}}}\right)^a, \tag{17}$$

where h_0 is the self-hardening coefficient, τ_0^{sat} is the saturation hardness and a is the hardening exponent. The hardening matrix $\mathbf{h}_{\beta\delta}$ is given by

$$\mathbf{h}_{\beta\delta} = \begin{cases} h_{\text{com}} & \text{if plates } \beta \text{ and } \delta \text{ are compatible} \\ h_{\text{com}} & \text{if plates } \beta \text{ and } \delta \text{ are incompatible} \end{cases}. \tag{18}$$

The material parameters used in this work and [40] are reproduced in Table 1 for reference.

References

[1] D. L. McDowell, Simulation-based strategies for microstructure-sensitive fatigue modeling, Mat Sci Eng A-Struct 468 (2007) 4–14.

[2] R. Prasannavenkatesan, C. P. Przybyla, N. Salajegheh, D. McDowell, Simulated extreme value fatigue sensitivity to inclusions and pores in martensitic gear steels, Eng Fract Mech 78 (6) (2011) 1140–1155.

[3] N. Salajegheh, R. Prasannavenkatesan, D. L. McDowell, G. B. Olson, H.-J. Jou, Finite element simulation of shielding/intensification effects of primary inclusion clusters in high strength steels under fatigue loading, J Eng Mater-T ASME 136 (3) (2014) 031003.

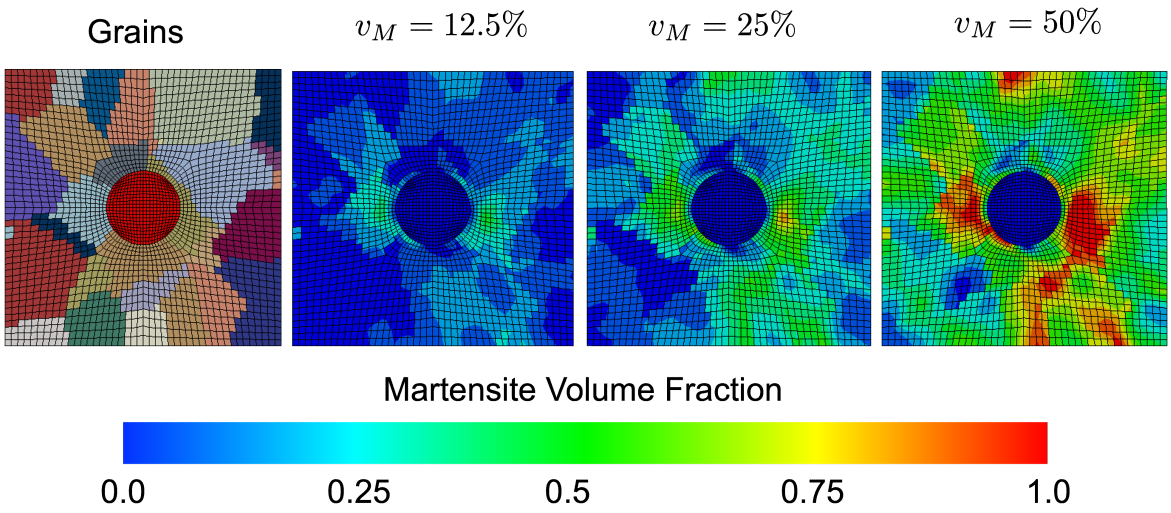

Figure 21: From left to right are shown the grain structure of the material then the local martensite volume fraction for 12.5%, 25%, and 50% global martensite volume fraction. Each image slice is in the $x-y$ plane at the center of the microstructure in the z-direction.

Parameter	Value	Parameter	Value
Austenite $\mathbb{C}_{11}$, GPa	130	h_{com}, MPa	2.125
Austenite $\mathbb{C}_{22}$, GPa	98	h_{incom}, MPa	8.5
Austenite $\mathbb{C}_{34}$, GPa	34	f_c, MPa	8.4
Austenite $\mathbf{A}_{\text{th}}$, K^{-1}	11×10^{-6}	$\dot{\gamma}_0$, s^{-1}	0.002
Martensite $\mathbf{A}_{\text{th}}$, K^{-1}	6.6×10^{-6}	m	0.02
θ_{T}, K	257	$\tau_0^{\text{time=0}}$, MPa	320
θ_0, K	277	h_0, MPa	500
λ_{T}, MPa	130	Q	1.4
a	0.125	τ_0^{sat}, MPa	900

Table 1: Parameters used in constitutive model

[4] J. A. Moore, D. Frankel, R. Prasannavenkatesan, A. G. Domel, G. B. Olson, W. K. Liu, A crystal plasticity-based study of the relationship between microstructure and ultra-high-cycle fatigue life in nickel titanium alloys, International Journal of Fatigue 91 (2016) 183–194.

[5] A. Muth, R. John, A. Pilchak, S. R. Kalidindi, D. L. McDowell, Analysis of fatigue indicator parameters for ti-6al-4v microstructures using extreme value statistics in the transition fatigue regime, International Journal of Fatigue 153 (2021) 106441.

[6] J. Zhang, R. Prasannavenkatesan, M. M. Shenoy, D. L. McDowell, Modeling fatigue crack nucleation at primary inclusions in carburized and shot-peened martensitic steel, Eng Fract Mech 76 (3) (2009) 315–334.

[7] G. M. Castelluccio, D. L. McDowell, Assessment of small fatigue crack growth driving forces in single crystals with and without slip bands, International journal of fracture 176 (1) (2012) 49–64.

[8] W. N. Findley, A theory for the effect of mean stress on fatigue of metals under combined torsion and axial load or bending, Journal of Engineering for Industry 81 (4) (1959) 301–305.

[9] R. Smith, P. Watson, T. Topper, et al., A stress-strain parameter for the fatigue of metals, Journal of Materials 5 (4) (1970) 767–778.

[10] M. W. Brown, K. Miller, A theory for fatigue failure under multiaxial stress-strain conditions, Proceedings of the Institution of Mechanical engineers 187 (1) (1973) 745–755.

[11] A. Fatemi, D. F. Socie, A critical plane approach to multiaxial fatigue damage including out-of-phase loading, Fatigue Fract Eng M 11 (3) (1988) 149–165.

[12] C. Bonsignore, Present and future approaches to lifetime prediction of superelastic nitinol, Theoretical and Applied Fracture Mechanics 92 (2017) 298–305.

[13] L. F. Coffin Jr, A study of the effects of cyclic thermal stresses on a ductile metal, Transactions of the American Society of Mechanical Engineers, New York 76 (1954) 931–950.

[14] S. S. Manson, Behavior of materials under conditions of thermal stress, Vol. 2933, National Advisory Committee for Aeronautics, 1953.

[15] J. Schijve, Fatigue of structures and materials, Springer Science & Business Media, 2008.

[16] G. B. Olson, M. Azrin, Transformation behavior of TRIP steels, Metallurgical transactions A 9 (5) (1978) 713–721.

[17] P. Adler, G. B. Olson, M. Stevens, G. Gallegos, On the constitutive relations for $\delta \rightarrow \alpha$ and $\alpha \rightarrow \delta$ martensitic transformation plasticity in plutonium alloys, Acta metallurgica et materialia 40 (5) (1992) 1073–1082.

[18] L. C. Brinson, One-dimensional constitutive behavior of shape memory alloys: thermomechanical derivation with non-constant material functions and redefined martensite internal variable, Journal of intelligent material systems and structures 4 (2) (1993) 229–242.

[19] D. C. Lagoudas, Shape memory alloys: modeling and engineering applications, Springer, 2008.

[20] J. Lankford, F. Kusenberger, Initiation of fatigue cracks in 4340 steel, Metallurgical Transactions 4 (2) (1973) 553–559.

[21] S. W. Robertson, M. Launey, O. Shelley, I. Ong, L. Vien, K. Senthilnathan, P. Saffari, S. Schlegel, A. R. Pelton, A statistical approach to understand the role of inclusions on the fatigue

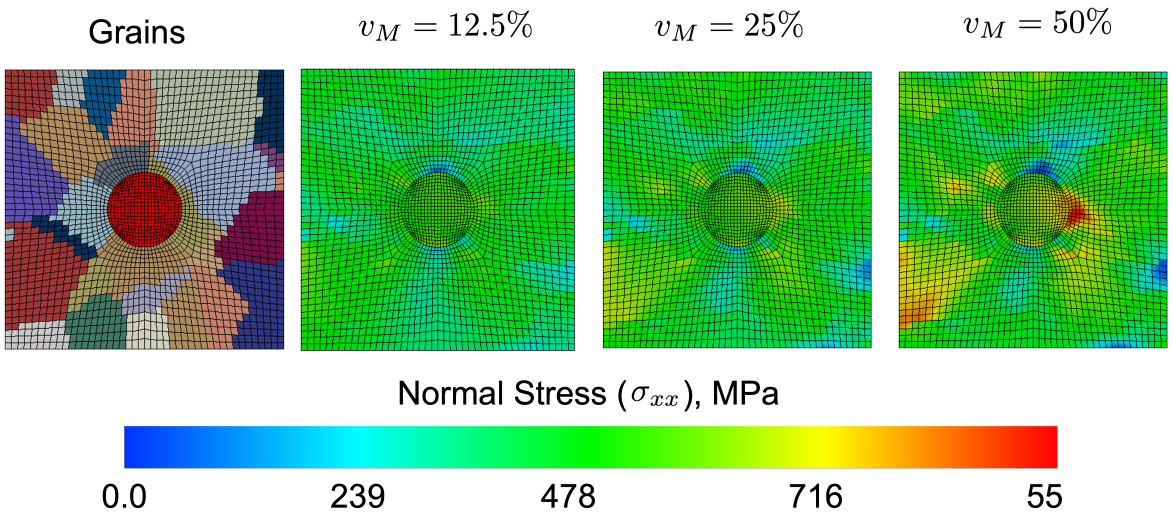

Figure 22: From left to right are shown the grain structure of the material then the normal stress in the x-direction produced from the load needed to induce 12.5%, 25%, and 50% global martensite volume fraction. Each image slice is in the $x - y$ plane at the center of the microstructure in the z-direction.

resistance of superelastic Nitinol wire and tubing, J Mech Behav Biomed Mater 51 (2015) 119–131.

[22] B. Liu, X. Yan, A new model of multiaxial fatigue life prediction with the influence of different mean stresses, International Journal of Damage Mechanics 28 (9) (2019) 1323–1343.

[23] H. Zhu, H. Wu, Y. Lu, Z. Zhong, A novel energy-based equivalent damage parameter for multiaxial fatigue life prediction, International Journal of Fatigue 121 (2019) 1–8.

[24] W. Sun, Y. Xu, C. Hu, X. Liu, Effect of film-hole configuration on creep rupture behavior of a second generation nickel-based single crystal superalloys, Materials Characterization 130 (2017) 298–310.

[25] A. Pelton, V. Schroeder, M. Mitchell, X.-Y. Gong, M. Barney, S. Robertson, Fatigue and durability of Nitinol stents, J Mech Behav Biomed 1 (2) (2008) 153–164.

[26] R. J. Asaro, Crystal plasticity, Journal of Applied Mechanics-Transactions of the ASME 50 (4B) (1983) 921–934.

[27] C. Przybyla, R. Prasannavenkatesan, N. Salajegheh, D. L. McDowell, Microstructure-sensitive modeling of high cycle fatigue, Int J Fatigue 32 (3) (2010) 512–525.

[28] N. Salajegheh, D. L. McDowell, Microstructure-sensitive weighted probability approach for modeling surface to bulk transition of high cycle fatigue failures dominated by primary inclusions, Int J Fatigue 59 (2014) 188–199.

[29] M. Shenoy, J. Zhang, D. L. McDowell, Estimating fatigue sensitivity to polycrystalline Ni-base superalloy microstructures using a computational approach, Fatigue & Fracture of Engineering Materials & Structures 30 (10) (2007) 889–904.

[30] G. Owolabi, H. Whitworth, Modeling and simulation of microstructurally small crack formation and growth in notched nickel-base superalloy component, Journal of Materials Science & Technology 30 (3) (2014) 203–212.

[31] G. Owolabi, R. Prasannavenkatesan, D. McDowell, Probabilistic framework for a microstructure-sensitive fatigue notch factor, Int J Fatigue 32 (8) (2010) 1378–1388.

[32] R. Kumar, A.-J. Wang, D. McDowell, Effects of microstructure variability on intrinsic fatigue resistance of nickel-base superalloys–a computational micromechanics approach, Int J Fracture 137 (1-4) (2006) 173–210.

[33] M. J. Mahtabi, N. Shamsaei, Multiaxial fatigue modeling for Nitinol shape memory alloys under in-phase loading, Journal of the Mechanical Behavior of Biomedical Materials 55 (2016) 236–249.

[34] O. L. Kafka, C. Yu, M. Shakoor, Z. Liu, G. J. Wagner, W. K. Liu, Data-driven mechanistic modeling of influence of microstructure on high-cycle fatigue life of nickel titanium, JOM 70 (7) (2018) 1154–1158.

[35] W. Yan, Y. Lian, C. Yu, O. L. Kafka, Z. Liu, W. K. Liu, G. J. Wagner, An integrated process–structure–property modeling framework for additive manufacturing, Computer Methods in Applied Mechanics and Engineering 339 (2018) 184–204.

[36] C. Yu, G. Kang, Q. Kan, D. Song, A micromechanical constitutive model based on crystal plasticity for thermo-mechanical cyclic deformation of NiTi shape memory alloys, Int J Plasticity 44 (2013) 161–191.

[37] M. J. Mahtabi, N. Shamsaei, B. Rutherford, Mean Strain Effects on the Fatigue Behavior of Superelastic Nitinol Alloys: An Experimental Investigation, Procedia Engineering 133 (2015) 646–654.

[38] S. Robertson, A. Pelton, R. Ritchie, Mechanical fatigue and fracture of nitinol, Int Mater Rev 57 (1) (2012) 1–37.

[39] A. Pelton, Nitinol fatigue: a review of microstructures and mechanisms, J Mater Eng Perform 20 (4-5) (2011) 613–617.

[40] S. Manchiraju, P. Anderson, Coupling between martensitic phase transformations and plasticity: A microstructure-based finite element model, Int J Plasticity 26 (10) (2010) 1508–1526.

[41] D. Peirce, R. Asaro, A. Needleman, An analysis of nonuniform and localized deformation in ductile single crystals, Acta metallurgica 30 (6) (1982) 1087–1119.

[42] P. Thamburaja, L. Anand, Polycrystalline shape-memory materials: effect of crystallographic texture, Journal of the Mechanics and Physics of Solids 49 (4) (2001) 709–737.

[43] L. C. Brinson, I. Schmidt, R. Lammering, Stress-induced transformation behavior of a polycrystalline NiTi shape memory alloy: micro and macromechanical investigations via in situ optical microscopy, Journal of the Mechanics and Physics of Solids

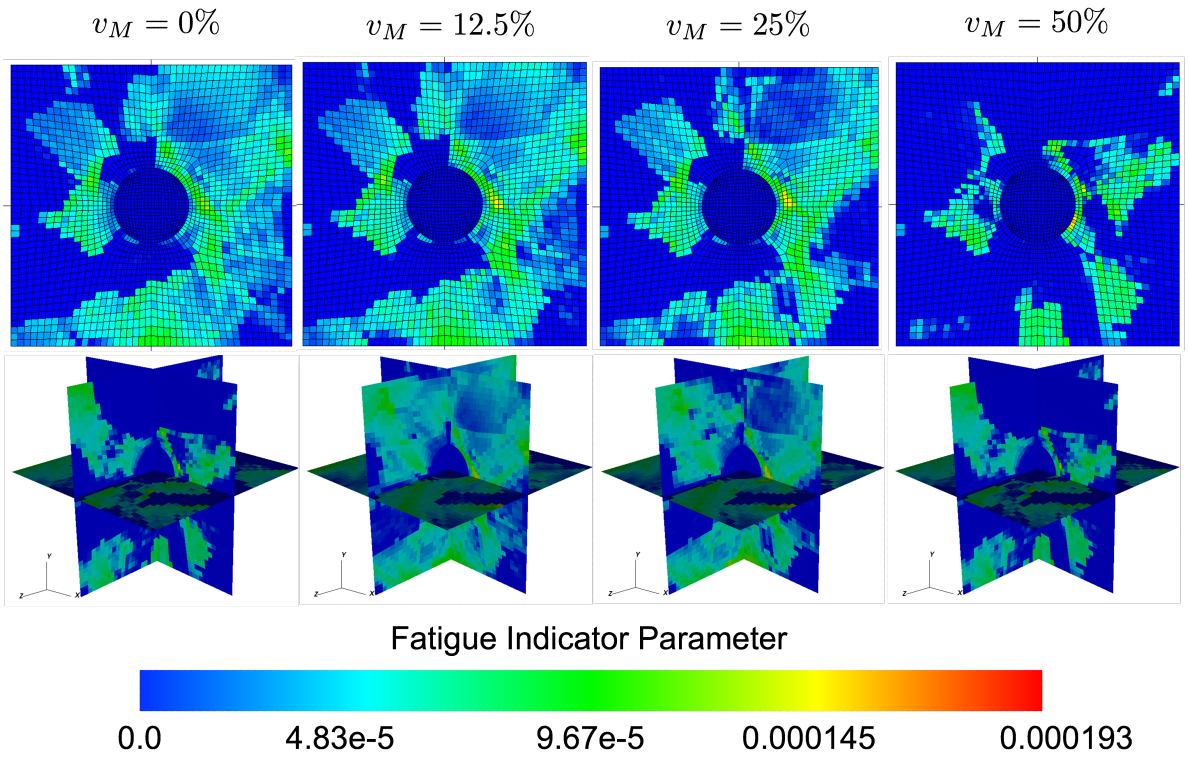

Figure 23: From left to right are shown the local FIP values for 0%, 12.5%, 25%, and 50% global martensite volume fraction loaded with 1% mean strain and 0.5% strain amplitude. Each image slice in the top row is in the $x-y$ plane at the center of the microstructure in the z-direction. Three planes slice the center of the structure in the bottom row.

52 (7) (2004) 1549–1571.

[44] G. M. Castelluccio, D. L. McDowell, Mesoscale modeling of microstructurally small fatigue cracks in metallic polycrystals, Materials Science and Engineering: A 598 (2014) 34–55.

[45] G. M. Castelluccio, D. L. McDowell, Microstructure and mesh sensitivities of mesoscale surrogate driving force measures for transgranular fatigue cracks in polycrystals, Materials Science and Engineering: A 639 (2015) 626–639.

[46] Fip with transform article code, `https://github.com/johnallanmoore/fipWithTransformArticle`, updated: 10-23-2023.

[47] S. Manchiraju, Modeling the coupling between martensitic phase transformation and plasticity in shape memory alloys, Ph.D. thesis, The Ohio State University (2011).

[48] S. Manchiraju, D. Gaydosh, O. Benafan, R. Noebe, R. Vaidyanathan, P. M. Anderson, Thermal cycling and isothermal deformation response of polycrystalline NiTi: Simulations vs. experiment, Acta Mater 59 (13) (2011) 5238–5249.

[49] R. Quey, P. Dawson, F. Barbe, Large-scale 3D random polycrystals for the finite element method: Generation, meshing and remeshing, Computer Methods in Applied Mechanics and Engineering 200 (17-20) (2011) 1729–1745.

[50] R. Quey, L. Renversade, Optimal polyhedral description of 3D polycrystals: Method and application to statistical and synchrotron x-ray diffraction data, Computer Methods in Applied Mechanics and Engineering 330 (2018) 308–333.

[51] R. Quey, A. Villani, C. Maurice, Nearly uniform sampling of crystal orientations, Journal of Applied Crystallography 51 (4) (2018) 1162–1173.

[52] M. Shenoy, R. Kumar, D. McDowell, Modeling effects of nonmetallic inclusions on LCF in DS nickel-base superalloys, Int J Fatigue 27 (2) (2005) 113–127.

[53] United States, and Battelle Memorial Institute. MMPDS-01 metallic materials properties development and standardization (MMPDS). [Washington, DC]: Federal aviation administration, 2008.

[54] K. Senthilnathan, A. Shamimi, C. Bonsignore, H. Paranjape, T. Duerig, Effect of prestrain on the fatigue life of superelastic nitinol, Journal of Materials Engineering and Performance 28 (10) (2019) 5946–5958.

[55] C. Yu, G. Kang, Q. Kan, Crystal plasticity based constitutive model of NiTi shape memory alloy considering different mechanisms of inelastic deformation, Int J Plasticity 54 (2014) 132–162.

[56] C. Yu, G. Kang, Q. Kan, Study on the rate-dependent cyclic deformation of super-elastic NiTi shape memory alloy based on a new crystal plasticity constitutive model, Int J Solids Struct 51 (25) (2014) 4386–4405.

[57] C. Yu, G. Kang, D. Song, Q. Kan, Effect of martensite reorientation and reorientation-induced plasticity on multiaxial transformation ratchetting of super-elastic NiTi shape memory alloy: New consideration in constitutive model, Int J Plasticity 67 (2015) 69–101.

[58] L. Xu, A. Solomou, T. Baxevanis, D. C. Lagoudas, A three-dimensional constitutive modeling for shape memory alloys considering two-way shape memory effect and transformation-

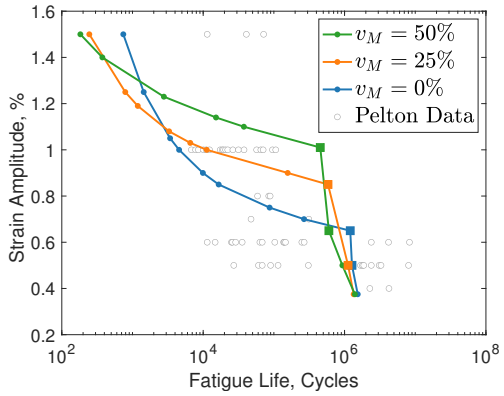

Figure 24: FIP values fit to Pelton et al.'s data [25]. The data between the square markers shows an increase in fatigue life with increased strain amplitude and is omitted. The connecting line between square datapoint is for visual reference only. For $v_M = 0\%, A = 1.4798$, $b = -0.6929$, $v_M = 25\%, A = 0.1600$, $b = -0.5310$, $v_M = 50\%, A = 0.0442$ $b = -0.4495$.

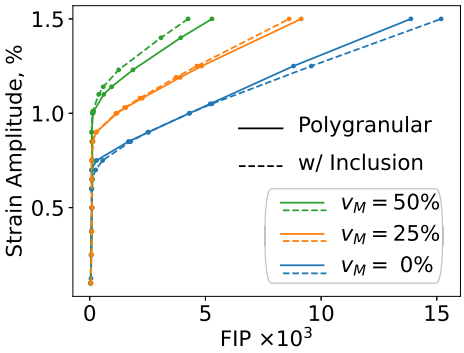

Figure 25: FIP values at various strain amplitudes and global martensite volume fractions for both the polygranular microstructures and polygranular microstructures with an inclusion. The mean strain for all simulations is 1%.

induced plasticity, in: AIAA Scitech 2019 Forum, 2019, p. 1195.

[59] J. Rusch, S. Manchiraju, J. A. Moore, Modeling of the transformation ratcheting of nitinol using computational crystal plasticity, in: 16th US National Congress on Computational Mechanics, 2021.

[60] A. Sengupta, P. Papadopoulos, Constitutive modeling and finite element approximation of B2-R-B19′ phase transformations in nitinol polycrystals, Computer methods in applied mechanics and engineering 198 (41-44) (2009) 3214–3227.